

RESEARCH ARTICLE

Accelerated carbonation of hardened cement paste: Quantification of calcium carbonate via ATR infrared spectroscopy

Jonas Kalkreuth | Angela Ullrich | Krassimir Garbev  | Daniela Merz | Peter Stemmermann | Dieter Stapf

Institute for Technical Chemistry,
Karlsruhe Institute of Technology,
Karlsruhe, Germany

Correspondence

Angela Ullrich and Krassimir Garbev,
Institute for Technical Chemistry,
Karlsruhe Institute of Technology,
Karlsruhe 76344, Germany.
Email: angela.ullrich@kit.edu;
krassimir.garbev@kit.edu

Funding information

German Helmholtz Association; Materials
and Technologies of the Energy Transition

Abstract

In context of carbon capture and storage in cement and concrete industry, there is a strong demand for fast, reliable, and low-cost CO₂ quantification methods. Attenuated total reflection infrared spectroscopy (ATR-IR) in conjunction with multivariate calibration via partial-least-squares regression was applied to quantify CaCO₃ in carbonated hardened Portland cement pastes, as this method shows great potential in the field of process control. Thermogravimetric analysis coupled with infrared spectrometry for the detection of the evolving gases was used as a reference for quantification. Three methods for the quantitative analysis with different partial-least-squares parameters were developed on a series of ground physical mixtures of slightly carbonated and highly carbonated hydrated cement pastes that had absorbed up to 77% of the theoretical capacity for CO₂. Additional samples for optimization and validation of the method were prepared by accelerated carbonation of cylindrical slices of hardened cement paste as a function of exposure time. In these experiments, the major CO₂ uptake occurs in the first 60 min until the formation of CaCO₃ layers limits the diffusion of CO₂ and Ca²⁺ ions. The developed partial-least-squares models provided low estimation errors of max. 1.5 wt% and high correlation coefficients above 99.5%. The validation covers a concentration range of 20–48 wt% of CaCO₃. Limitations of the method are discussed.

KEYWORDS

ATR-IR spectroscopy, carbonation, cement pastes, multivariate partial-least-squares regression, TG-FTIR

1 | INTRODUCTION

As cement production is associated with CO₂ emissions that contribute 5%–8% to the global greenhouse

gas (GHG) release worldwide,¹ different approaches to reduce the CO₂ emissions are proposed. These include extended service life, optimization of the cement content in concrete structures,² or extended use of supplementary

This is an open access article under the terms of the [Creative Commons Attribution-NonCommercial-NoDerivs](https://creativecommons.org/licenses/by-nc-nd/4.0/) License, which permits use and distribution in any medium, provided the original work is properly cited, the use is non-commercial and no modifications or adaptations are made.

© 2023 The Authors. *Journal of the American Ceramic Society* published by Wiley Periodicals LLC on behalf of American Ceramic Society.

cementitious materials (SCM), for example, calcined clays and limestone.³ Nevertheless, the use of some SCMs may be confined due to performance restrictions. With respect to process emissions, a particularly suitable approach for the reduction of GHG seems to be carbon capture and storage (CCS).^{4–6} An extended review of possible CCS technologies and methods for CO₂ mineralization in the chain of cement and concrete industry is given in Ref. (7). Recently, in particular the utilization of carbonated fines from recycled concrete has gained interest.^{4,8}

The carbonation of concrete in air is extremely slow due to the low CO₂ content (400 ppm). Nevertheless, it can be detected within a day.⁹ Increased CO₂ concentrations of up to 3%–4% accelerate the carbonation of Portland cement pastes significantly and do not seem to change the microstructure of the hardened cement paste (HCP) substantially.¹⁰ Different methods for accelerated carbonation are proposed.¹¹ Factors influencing the rate of carbonation include relative humidity (RH), temperature, porosity, cement type and CO₂ concentration (cCO₂), pressure, duration, etc. The influence of RH at constant cCO₂ of 3% was studied by Suda et al.^{12,13} Galan et al. followed the carbonation of HCP at constant RH and 100% CO₂¹⁴ and as a function of RH, water to cement ratio (*w/c*), and different cCO₂.¹⁵ The utilization of CO₂ for carbonation curing proposed in the 1970s¹⁶ has also been intensively investigated recently as a method for CO₂ sequestration.^{17,18} Skocek et al. demonstrate the influence of the particle size on the reaction kinetics of the carbonation process of recycled concrete fines. While fine particles undergo complete carbonation at relative low temperature and PCO₂ (80°C, 2 bar), the larger aggregates seem to need significantly higher temperature and pressure (140°C–180°C and *P* > 8 bar).⁴

Different aspects of the carbonation of the cement paste are described in the work of Savija and Lukovic.¹⁹ Due to the high pH of cement paste and the uptake of CO₂ from air, carbonation is very favored upon addition of H₂O. The main reactions include the transformation of Ca(OH)₂ (CH) to CaCO₃, which is favored in comparison with the remaining hydration phases (standard cement nomenclature is used throughout the manuscript where C = CaO, S = SiO₂, H = H₂O, A = Al₂O₃, \$ = SO₃, F = Fe₂O₃). The carbonation of calcium-silicate-hydrate (C-S-H) includes decalcification and silicate polymerization in several steps until the subsequent formation of silica gel.^{20,21}

Particularly important is the use of quick, precise, and reliable analytical methods for the assessment of the degree of carbonation in hardened cement pastes and the description of its kinetics.²² The methods used so far only partially fulfill this requirement. Along with the phenolphthalein staining method for imaging the carbonation

depth,²³ mercury intrusion porosimetry and scanning electron microscopy were employed to illustrate the change in the microstructure of carbonated pastes.²² ²⁹Si magic angle spinning nuclear magnetic resonance (MAS NMR) data confirm the polymerization of the silicate units.^{9,20,24} Although widely used, the applicability of X-ray diffraction (XRD) remains limited due to the presence of both, amorphous CH interlaced with C-S-H and amorphous CaCO₃, especially in the early stages of carbonation.²⁵ Thermogravimetry (TG) is a reliable quantification method. However, it is time-consuming and there are possible effects of superimposition of H₂O and CO₂ loss in the 400°C–600°C range as well as of CO₂ and SO₂ loss at higher temperatures. Therefore, it is necessary to couple TG either to a mass spectrometer (MS), or to a Fourier-transform-infrared-spectrometer (FTIR) in order to gain information about the chemistry and to determine the exact temperature range of a certain decomposition step. This is a prerequisite for further quantification.²⁶ Furthermore, the use of attenuated total reflection infrared spectroscopy (ATR-IR) for rapid evaluation of the carbonate content offers great opportunities due to the possibility of quick measurements and sensitivity to the different CaCO₃ polymorphs, amorphous calcium carbonate (ACC),²⁷ calcite, vaterite, and aragonite.²⁸ ATR-IR was successfully utilized previously to study cement hydration in situ and ex situ.^{29–31} Especially the advantages of the ATR-IR in terms of simplicity, sample preparation, and in combination with multivariate calibration are shown in the pioneering work of Mendes dos Santos et al.³²

This work aims to develop quick and reliable methods for the quantitative analysis of CaCO₃ in HCP exposed to accelerated carbonation at 8 bar CO₂ pressure and 170°C under hydrothermal conditions. The choice of these parameters is based on the results of Ref. (19) also taking in account the size of our samples. The methods rely on partial-least-squares (PLS) regression in conjunction with ATR-IR spectroscopy. The quantification of the calibration samples is performed by TG-FTIR. In addition, the influence of the duration of CO₂ treatment on the degree of HCP carbonation was investigated.

2 | MATERIALS AND METHODS

2.1 | Preparation and carbonation of hardened cement paste

CEM-I cement paste (Dyckerhoff white; 42.5/R pure Portland cement; *w/c* = 0.5) was prepared using a mortar-mixer (3 min 140 U/min, 2 min 285 U/min). The mixture was poured into cylindrical PVC molds (diameter 3 cm, height 2.5 cm), which were covered with plastic foil for

24 h to prevent dehydration. Subsequently, the HCP was cured under water for 28 days. For the calibration mixtures, multiple blocks of HCP were coarsely crushed with a hammer (Supplementary Material S1). Half of the material was dried under vacuum, ground for 10 min at 300 U/min in a planetary ball mill Pulverisette 5 (Fritsch GmbH, Idar-Oberstein, Germany), and stored in a nitrogen atmosphere to prevent carbonation (slightly carbonated sample CS01). The second part was carbonated with some additional water (50 mL) in an autoclave and was subsequently ground in a planetary ball mill under the aforementioned conditions (highly carbonated sample CS11). The carbonation was carried out in a stainless steel high pressure reactor BR 500 (Berghof products+instruments, Eningen, Germany; Supplementary Material S1) with a duration of 52 h at 170°C and 8 bar CO₂. Eleven calibration samples (3 g) with different CS01:CS11 ratios (100:0, 90:10, . . . 0:100) of ground slightly and highly carbonated (sc and hc) HCP were homogenized in an agate mortar. In addition, one sample for cross-validation was prepared with a CS01:CS11 ratio of 85:15 (Supplementary Material S2).

Furthermore, sliced specimens (3 cm diameter, 0.5 cm height) were cut out of the residual blocks using a high precision saw (ISO-MET 1000, Bühler, ITW Test & Measurement GmbH, Leinfelden-Echterdingen, Germany). These specimens were placed in the preheated (170°C) autoclave and were carbonated at 8 bar CO₂. CO₂ exposure times were 0, 10, 20, 30, 60, 90, and 180 min (samples V01–12). Subsequently, the specimens were vacuum dried in the autoclave (105°C) for 3 h and stored in a nitrogen atmosphere to prevent further carbonation until analysis. Besides the investigation of the influence of CO₂ exposure time on the degree of carbonation, these specimens were also used for the validation of the developed ATR-IR calibrations, and to cover a wider range of different CaCO₃ concentrations in the calibration. In general, two samples per specimen, one in the center and one from the outer rim, were taken with a precision drill for analysis (Supplementary Material S1). The samples exposed for 10, 90, and 180 min were completely homogenized for determination of the precision (V04, V11), and the hydrated sample before carbonation was measured threefold (Supplementary Material S3).

2.2 | Sample characterization

2.2.1 | X-ray fluorescence (XRF) analysis

The loss of ignition (LoI) was determined according to DIN 196-2. XRF analysis was carried out according to DIN 51729-10 on a “S8 Tiger 3K” wavelength dispersive spectrometer (Bruker AXS GmbH, Karlsruhe, Germany)

with a rhodium X-ray tube and scintillation counter detectors with LiF(220), XS-Ge-C, PET, XS-55, and XS-CEM analyzer crystals.

2.2.2 | TG analysis

TG measurements were carried out with a thermo-balance Jupiter STA 449 F3 (NETZSCH, Selb, Germany) equipped with platinum furnace operated in the range 25°C–1400°C. Sample amounts of about 10 mg were measured in Al₂O₃ crucibles with a heating rate of 10 K/min under N₂ purge and protective gas flow of 60 mL/min. The TG data related to the evolution of CO₂ was evaluated by application of the tangential Marsh method implemented in Netzsch Proteus 8.0.1. and by integration of the differential thermogravimetry (DTG) peak of CO₂ release. The mean of both methods with its standard error was determined and the CaCO₃ contents were calculated according to the molecular weights. Two measurements were performed for the calibration samples and six measurements for the samples used for determination of the precision (TG and TG-FTIR).

2.2.3 | TG-FTIR analysis

The TG analyzer was coupled to a Tensor 27 spectrometer (Bruker-Optics, Ettlingen, Germany) via a transfer gas line and FTIR gas cell, both kept at a constant temperature of 200°C. The gas detection was performed with a liquid nitrogen cooled MCT (mercury cadmium telluride) detector. Spectra with 32 scans and spectral resolution of 4 cm⁻¹ in the range 600–4000 cm⁻¹ were acquired. The calibration of the FTIR spectrometer was carried out with certified test gases in the validity range of Beer–Lamberts law. The quantification of CO₂ and CaCO₃ respectively was performed using the method developed by Merz et al.²⁵ (Supplementary Material S4).

2.2.4 | ATR-IR analysis

ATR-IR measurements were performed on a Tensor II spectrometer (Bruker-Optics, Ettlingen, Germany) with a deuterated triglycine sulfate (DTGS) detector and a Golden Gate ATR cell with a diamond crystal (Specac LTD, Orpington, UK). Spectra with 64 scans and a spectral resolution of 2 cm⁻¹ in the range 400–4000 cm⁻¹ were acquired per measurement. Sample pellets were prepared by compression of 80 mg sample in a Quick-Table-Top-Press (International Crystal Laboratories, Garfield, NJ, USA). Three pellets per sample were prepared and measured.

For better understanding of the sample spectra, synthetic pure clinker phases (C_3S , C_2S , C_3A),³³ Ca-sulfates (anhydrite, basanite, gypsum, p.a., MERCK), synthetic C-S-H ($C/S = 1.5$, $C/S = 0.67$, where C/S indicates the molar ratio CaO/SiO_2),³⁴ AFt (ettringite), AFm (monocarbonate, monosulfate, courtesy H. Pöllmann), Ca-carbonates (calcite p.a. MERCK, aragonite, Oued Amahmaje, Marokko), and highly disperse silica (Aerosil 200, Evonik) were measured.

2.3 | ATR-IR calibration and PLS regression

The PLS regression was performed for 12 calibration samples (Supplementary Material S2) via the Quant 2 package for the OPUS V.8.1 program by Bruker (Bruker-Optics, Ettlingen, Germany). Multiple methods with different spectral ranges as well as different combinations of pre-processing of the spectra were developed. Possible pre-processing was linear offset subtraction (LOS), straight-line subtraction (SLS), standard normal variate normalization (SNV), minimum-maximum-normalization (MMN), multiplicative scatter correction (MSC) and 1st derivative (1.DER). The quality of the PLS regression was assessed with the implemented cross-validation of the “Quant 2” package as well as by an external validation regarding the TG-FTIR reference. Eight specimens with different CO_2 exposure times were used for the validation to ensure a sufficiently wide range of concentration for the validation (Supplementary Material S3). Accuracy (deviation between prediction and reference) and precision (variances of six replicate measurements) of the developed methods were examined and tested for statistical significance with a paired t -test and F -test, respectively. The precision of the methods was examined at two $CaCO_3$ concentrations using six replicate measurements per concentration. To optimize the developed methods, eight of the validation samples were implemented in the data set for the PLS regression and the optimized methods were validated with three validation samples at different concentrations.

3 | RESULTS AND DISCUSSION

3.1 | Characterization of the initial CEM-I cement

The characterization of the initial CEM-I cement was carried out using TG, XRF (Table 1), and ATR-IR analysis. Excess water absorbed from the atmosphere evaporates up to $100^\circ C$ and results in 0.4 wt% weight loss (wl).

TABLE 1 Thermal analysis of the initial CEM-I sample. Mean values of the evaluation by tangential Marsh method and by integration of the DTG peak are given with their estimated standard deviation (e.s.d.; wl = weight loss; $H_2O_{total} = wl\ 29^\circ C - 900^\circ C - CO_2$). LoI and oxide contents were determined by XRF analysis.

Compound	wt%	e.s.d.
$H_2O_{Ca(OH)_2}$	0.36	0.09
$Ca(OH)_2$	1.5	0.4
CO_2	2.1	0.1
$CaCO_3$	4.7	0.3
H_2O_{total}	1.25	–
wl $29^\circ C - 950^\circ C$	3.34	–
LoI	3.36	–
CaO	65.2	0.2
SiO_2	21.1	0.04
Al_2O_3	4.46	0.003
SO_3	2.90	0.002
MgO	0.80	0.01
K_2O	0.64	0.001
Fe_2O_3	0.22	0.001
TiO_2	0.11	0.001

Small amounts of cement hydration products (C-S-H, AFt, and AFm) dehydrate up to around $380^\circ C$,³⁵ as well as crystallized water of gypsum ($CaSO_4 \cdot 2H_2O$) resulting in an additional 0.6 wt% loss. Total amounts of $Ca(OH)_2$ and $CaCO_3$ in the nonhydrated sample were calculated from the mass losses determined by the tangential method within the temperature ranges $350^\circ C - 420^\circ C$ and $500^\circ C - 780^\circ C$ for $Ca(OH)_2$ and $CaCO_3$, respectively.³⁶ The corresponding loss of 0.4 wt% calculates to 1.5 wt% $Ca(OH)_2$, and that of 2.1 wt% reveals the presence of 4.7 wt% $CaCO_3$. While presence of 1.5 wt% portlandite is very likely to be due to prehydration of free lime occurring at $RH > 11\%$,³⁷ the detection of $CaCO_3$ in such high quantities implies that calcite was added as minor component in the cement. The total weight loss up to $950^\circ C$ is consistent with the LoI within ± 0.1 wt%.

The main oxide contents of the CEM-I sample are CaO (C) and SiO_2 (S) besides small amounts (< 5 wt%) of Al_2O_3 and SO_3 . As expected for a CEM-I white, the Fe_2O_3 content is rather low (0.2 wt%). A low TiO_2 content (0.1 wt%) for adjustment of the white value is also typical for white cement. The C/S ratio is 3.3.

Figure 1 shows the ATR spectrum of the cement sample along with the single spectra of its main components. The cement sample shows main absorption in the range $800 - 1000\ cm^{-1}$ typical for symmetrical and asymmetrical Si-O stretching vibrations ν_1 and ν_3 in C_3S and C_2S . Additionally, C_3A also contributes with Al-O stretching bands mostly to lower frequencies. The absorption in the range

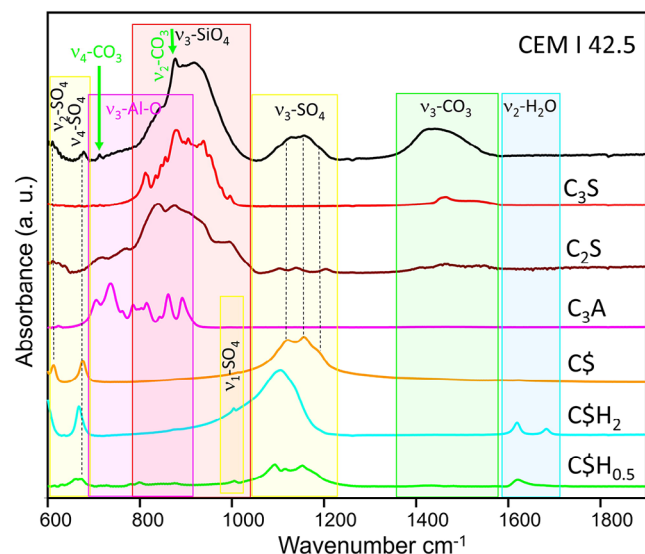


FIGURE 1 ATR spectra of the CEM-I 42.5 with single spectra of its main components.

TABLE 2 H₂O and CO₂ contents of scHCP (CS01) and hcHCP (CS11) determined by TG and TG-FTIR analysis. The errors describe the standard deviations of the mean of two measurements. H₂O_{total} is the mean of w1 29°C–900°C—CO₂ determined by TG-FTIR.

Compound	CS01	CS11
H ₂ O _{total}	17.1 (1)	6.97 (4)
CO ₂ TG (wt%)	1.2 (2)	28.2 (5)
CO ₂ TG-FTIR (wt%)	1.1 (1)	26.9 (5)

1000–1200 cm⁻¹ is due to S-O asymmetrical (ν_3) stretching in CaSO₄ and its hydrated phases basanite and gypsum. Comparison with the spectra of these phases shows that anhydrite with bands at 612 cm⁻¹ (ν_2), 676 cm⁻¹ (ν_4), and the ν_3 triplet at 1120, 1156, and 1188 cm⁻¹ is the main contributor to the absorption. The broad absorption between 1350 and 1550 cm⁻¹ as well as the sharp bands at 712 cm⁻¹ and 873 cm⁻¹ confirm the presence of calcite.

3.2 | Effects of CO₂ on HCP

Table 2 summarizes the H₂O and CO₂ contents for samples of scHCP (28 days hydration) and hcHCP (52 h carbonation). The H₂O content is determined by TG. For the investigation of the CO₂ contents in all hydrated and carbonated samples, the results by means of both techniques—TG and TG-FTIR—are provided. Comparison and advances of TG-FTIR and hence the selection of the reference values for the development of the ATR methods will be discussed in Section 3.4.1. The carbonation of the hcHCP is clearly visible in the high CO₂ contents whereas the content of H₂O decreases.

The ATR-IR spectrum of scHCP (Figure 2) is characterized by the absorption bands due to the asymmetric Si-O stretching vibration (958 cm⁻¹) of C-S-H,^{38,39} the O-H stretching (3643 cm⁻¹) of Ca(OH)₂,⁴⁰ and the bending vibration (1600–1700 cm⁻¹) as well as the symmetric and asymmetric stretching vibration (3000–3550 cm⁻¹) of crystalline bound water.³⁰ For comparison, the ATR spectra of two synthetic C-S-H phases with different C/S ratios of 1.5 and 0.67 are given in Figure 2. The main Si-O band is positioned at 950 and 965 cm⁻¹, respectively showing the increase of the vibrational frequency with lowering of the C/S ratio mostly influenced by increased silicate polymerization. Additionally, the broad absorption band at 1125 cm⁻¹ could be assigned to the asymmetric stretching vibration ν_3 -(SO₄) (1125 cm⁻¹) in ettringite.^{41,42} On a one hand, the presence of the out-of-plane bending vibration (800–880 cm⁻¹) and the asymmetric stretching vibration (1300–1600 cm⁻¹) of CO₃²⁻^{43,44} could be once again assigned to calcite as minor additional component in the cement. On the other hand, a closer examination reveals the presence of monocarbonate (3CaO·Al₂O₃·CaCO₃·11H₂O) manifested by its strong ν_2 -(CO₃) band at 873 cm⁻¹ and the pronounced shoulder at 1365 cm⁻¹ in the range of ν_3 -(CO₃) modes with additional bands at 1415 and 1480 cm⁻¹. The ν_3 -CO₃ mode of monocarbonate shows typical splitting giving rise to bands at 1360 and 1418 cm⁻¹.⁴⁵ Therefore, the peak observed at 1415 cm⁻¹ is strongly influenced by monocarbonate. The chemical environment of the carbonate ion and the respective proportions of different CaCO₃ modifications influence the shape of the asymmetric stretching vibration.⁴⁶ Generally, the absorption in this range is possibly due to the presence of a mixture of mainly monocarbonate with additions of ACC and low crystalline vaterite, calcite, and aragonite. Considering further the OH range once again, the presence of monocarbonate is confirmed by the small bands at 3520 and 3670 cm⁻¹.

Figure 3 shows the ATR spectra of hcHCP (CS11). Additionally, the spectra of synthetic calcite, natural aragonite, and highly dispersed silica (Aerosil) are given. As a result of carbonation, the mass fraction of CaCO₃ increases, which leads to an increase in the absorption bands of the corresponding carbonate vibrations (712, 873, and 1300–1600 cm⁻¹) while the intensity of the O-H stretching vibration of Ca(OH)₂ decreases due to the chemical reaction of Ca(OH)₂ and CO₂ to CaCO₃. The reaction of CO₂ with the C-S-H leads to a decalcification and polymerization of the C-S-H phase and the formation of CaCO₃ as well as amorphous SiO₂ gel.¹⁹ This effect can be seen in the shift of the asymmetric stretching vibration ν_3 -(Si-O) of C-S-H- at 958 cm⁻¹ to higher frequencies eventually leading to broad absorption centered at 1070 cm⁻¹, which corresponds to the asymmetrical Si-O stretching vibration of

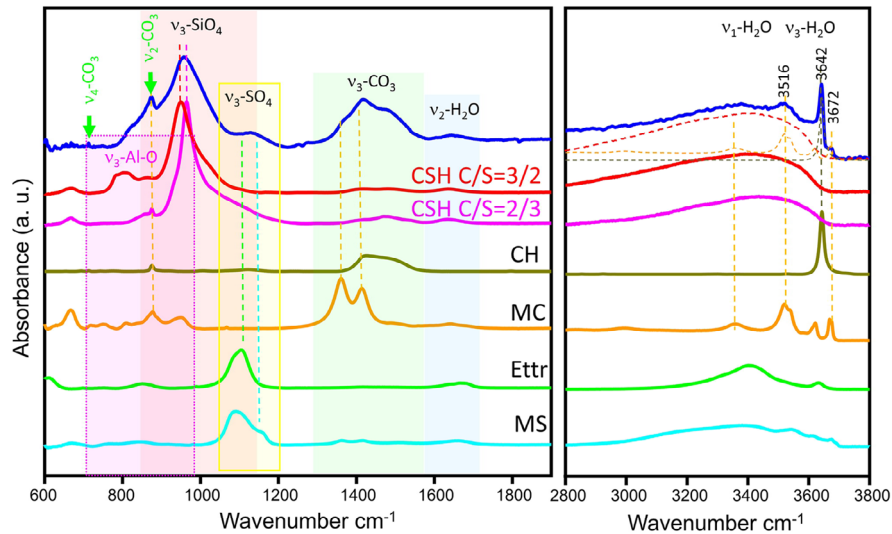


FIGURE 2 ATR spectra of 28-day-old schHCP (CS01). Spectra of pure components are also shown: C-S-H phases with C/S of 3/2 and 2/3, portlandite (CH), monocarbonate (MC), ettringite (Ettr), and monosulphate (MS) (from top to bottom).

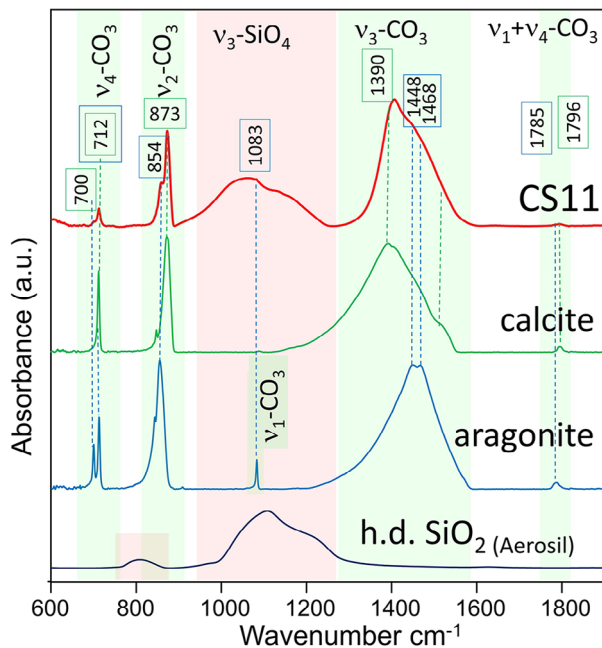


FIGURE 3 From top to bottom: ATR spectra of the hchHCP (CS11), pure calcite (p.a. MERCK), aragonite (natural sample), and amorphous highly disperse silica (Aerosil).

the SiO_2 gel²⁸ matching the spectrum of highly disperse silica shown in Figure 3 (bottom). The polymerization of the SiO_2 gel restricts the mobility of the molecules, which shifts the absorption band toward higher wavenumbers since more energy is required for the vibrational excitation. The reaction of the C-S-H with CO_2 is manifested also by the strong intensity decrease of its typical water bands. Carbonation also leads to the formation of different CaCO_3 polymorphs. The spectrum of CS11 shows the

increased formation of calcite manifested by the bands at 712 cm^{-1} (ν_4), 873 cm^{-1} (ν_2) and $1390\text{--}1400\text{ cm}^{-1}$ (ν_3). Additional absorption bands with lower intensity at 700 cm^{-1} , 856 cm^{-1} and 1083 cm^{-1} correspond to the formation of aragonite. The broadening of the absorption bands due to ν_3 mode to higher frequencies is also due to the presence of aragonite (bands at 1448 and 1468 cm^{-1}). The different point symmetry of calcite (D3) and aragonite (Cs) promote different selection rules for Raman and IR activity⁴⁷ resulting in splitting of the ν_4 mode into bands at 700 and 712 cm^{-1} and in IR activity of the symmetrical ν_1 -C-O stretching mode at 1083 cm^{-1} of aragonite,⁴⁸ which is IR silent in calcite.⁴⁹ The combination mode ($\nu_1 + \nu_4$) is also influenced by the selection rules giving rise to a sharp band with low intensity at 1785 and 1796 cm^{-1} in the spectra of aragonite and calcite, respectively. The comparison of the spectra in Figure 3 shows a clear dominance of calcite over aragonite in sample CS11.

3.3 | Influence of the CO_2 exposure time on the carbonation degree of HCP

In general, two samples were analyzed per sliced specimen (V01–V12), one from the center and one from the rim. The CaCO_3 content was determined by quantitative TG and coupled FTIR analysis. The CaCO_3 content on the outer specimens was higher because CO_2 diffuses from the rim to the interior of the specimen (Supplementary Material S3). However, for the further evaluation of the CO_2 -exposure times, the arithmetic means and the standard error of the mean were calculated. These values

were used to determine the CO₂ uptake per kg dry cement (without H₂O and CO₂) according to:

$$\begin{aligned} \text{CO}_{2,\text{uptake HCP}} \text{ (g/kg}_{\text{CEM-I}}\text{)} \\ = \frac{m_{\text{CO}_2,\text{HCP}} \text{ (wt\%)}}{(100 - m_{\text{H}_2\text{O,HCP}} \text{ (wt\%)} - m_{\text{CO}_2,\text{HCP}} \text{ (wt\%)})} \\ \cdot 100 \cdot 10 - \text{CO}_{2,\text{uptake CEM-I}} \text{ (g/kg)}, \end{aligned} \quad (1)$$

$$\begin{aligned} \text{CO}_{2,\text{uptake CEM-I}} \text{ (g/kg)} \\ = \frac{m_{\text{CO}_2,\text{CEM-I}} \text{ (wt\%)}}{(100 - m_{\text{H}_2\text{O,CEM-I}} \text{ (wt\%)} - m_{\text{CO}_2,\text{CEM-I}} \text{ (wt\%)})} \cdot 100 \cdot 10. \end{aligned} \quad (2)$$

The CO₂ uptake was calculated for both the m_{CO₂} values determined by TA and the ones determined by FTIR. The m_{H₂O} content was calculated by subtraction of m_{CO₂} from the weight loss between 29°C and 900°C.

The CO₂ uptake efficiency was calculated regarding the theoretical maximum CO₂ uptake (CO_{2,max}) according to:

$$\text{CO}_{2,\text{Eff.}} \text{ (\%)} = \frac{\text{CO}_{2,\text{uptake HCP}}}{\text{CO}_{2,\text{max}}} \cdot 100. \quad (3)$$

The equation of Huntzinger et al.⁵⁰ was modified to calculate the maximum amount of CO₂, which can be incorporated per kg dry CEM-I by chemical reaction.

$$\text{CO}_{2,\text{max}} \text{ (g/kg}_{\text{CEM-I dry}}\text{)} = \frac{(0.785 \text{ (CaO} - 0.56 \text{ CaCO}_3 - 0.7 \text{ SO}_3) + 1.091 \text{ MgO} + 0.71 \text{ Na}_2\text{O} + 0.468 \text{ K}_2\text{O})}{100 - m_{\text{CO}_2,\text{CEM-I}} \text{ (wt\%)} - m_{\text{H}_2\text{O,CEM-I}} \text{ (wt\%)}} \cdot 100 \cdot 10 \quad (4)$$

The individual amounts of the corresponding oxides determined by XRF analysis of the CEM-I cement (Table 1) were used in the calculation. CO₂ uptake and uptake efficiency regarding the carbonation time are illustrated in Figure 4. Slightly negative values for CO₂ uptake and uptake efficiency were calculated for the hydrated samples. This reflects the error due to sample inhomogeneities and sample preparation in air which result in normalized CO₂ contents of 1.9 and 0.6–0.8 wt% for the dry CEM-I sample and the hydrated samples, respectively.

The carbonation rate is highest within the first 30 min; it decelerates between 30 and 60 min while only small differences were observed between 60 and 90 min. However, the standard deviation decreases between 60 and 180 min as the difference between CO₂ uptake in the center and outer sample decreases. Sixty percent of the CO₂

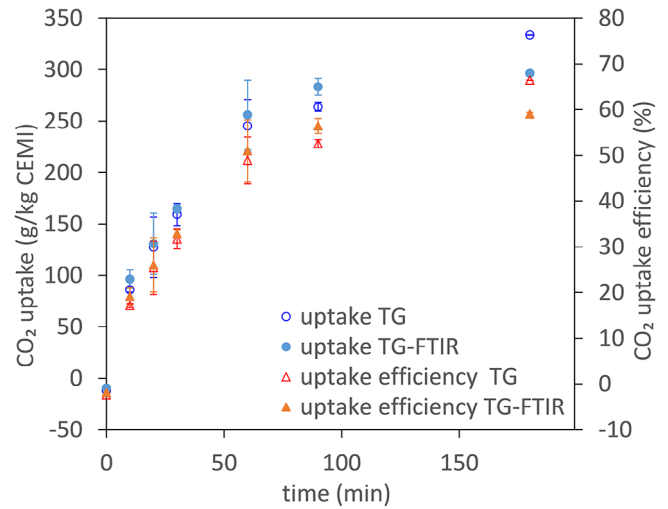


FIGURE 4 Temporal evolution of the CO₂ uptake and CO₂ uptake efficiency determined by TG and TG-FTIR at 170°C and 8 bar CO₂ (mean values with standard deviation). See Section 3.4.1 for the discussion about the analytic methods.

uptake occurs within the first 30 min, 90% within the first 60 min. Fang and Chang⁵¹ observed similar results after accelerated carbonation for 2 h (water/solid ratio = 0.15, P_{CO₂} = 0.2 MPa). Wang et al.⁵² who investigated the effect of pressure, temperature, and water/binder ratio on the CO₂ uptake of 20 mm HCP cubes during mineral carbonation curing achieved 70% CO₂ uptake efficiency within

the first 20 min and observed a convergence of the carbonation rate against a plateau after 90–120 min. The reduction of the carbonation rate with increasing carbonation time may be due to “clogging,” that is, the formation of CaCO₃ layers, inhibiting the diffusion of CO₂ and Ca²⁺ ions from the hardened cement paste.⁵³ As soon as all reactive surfaces are saturated with CaCO₃, the carbonation reaction stops.⁵⁴ Wang et al.⁵⁰ discovered that an increase in CO₂ pressure leads to an increase in carbonation because CO₂ penetrates deeper into the interior of the hardened cement paste while increasing the solubility of CO₂ in water. However, the evolution of the carbonation rate was similar, decreasing with increasing CO₂ exposure time. Thus, higher CO₂ pressures may offer the advantage that CO₂ diffuses deeper into the hardened cement paste before the outer pores close due to the formation of CaCO₃.⁵⁵

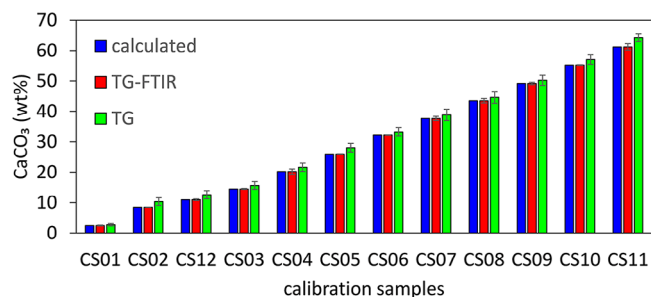


FIGURE 5 Comparison between expected values and reference methods: TG and TG-FTIR. Error bars describe the standard error of the mean of two measurements (TG and TG-FTIR).

In comparison, the sample carbonated for the calibration mixtures that was crushed before CO₂ exposure of 52 h reached 77%–81% (TG-FTIR and TG) CO₂ uptake efficiency.

3.4 | Quantification of CaCO₃ in hardened cement paste via ATR-IR spectroscopy in conjunction with multivariate PLS regression

3.4.1 | Method development and validation

The basic principle of the quantitative multivariate methods lies in the measurement of calibration samples with contents covering the whole range of interest by an independent method. In this work, the samples were prepared by mixing the weighted proportions of hcHCP with scHCP. The resulting mixtures were analyzed by quantitative TG and TG-FTIR. The results from these techniques and the expected (weighted) values are compared in Figure 5 (Supplementary Material S2). As the TG-FTIR method delivers the most reliable results for the determination of the quantity of CaCO₃, these values were used for further method development. Thermogravimetry alone proves to be insufficient due to the difficulty to differentiate between CO₂, H₂O, and SO₃ losses, especially in the temperature range between 450°C and 600°C. Therefore, TG tends to overestimate the CO₂ loss at the cost of H₂O.

In order to guarantee a reliable prediction of the ATR-IR calibration model, the calibration mixtures must reproduce the changes of the experimentally measured ATR-IR spectra upon carbonation. Figure 6 illustrates the evolution of the ATR-IR spectra measured on samples from carbonation experiments with CO₂ exposure time compared to the prepared calibration mixtures. There is a high accordance between the experimental ATR-IR spectra and those of the calibration mixtures. Increasing fractions of highly

carbonated powder led to an increase in the intensity of the asymmetric stretching vibration (1300–1600 cm⁻¹) and the bending vibrations (712 and 873 cm⁻¹) of the carbonate ion, while the absorption band of the O-H stretching vibration of Ca(OH)₂ (3642 cm⁻¹) and the asymmetric Si-O stretching vibration of the C-S-H (958 cm⁻¹) lose intensity. The shift of the initial Si-O stretching vibration of the C-S-H (958 cm⁻¹) toward higher wavenumbers, as a result of the decalcification and polymerization of the C-S-H, could also be reproduced.

Several quantification methods were developed upon varying both spectral ranges and preprocessing procedures offered by the “Quant 2” package. The quality of the PLS regression was evaluated by the implemented cross-validation. The three “best” methods regarding the smallest deviation to the reference are listed in Table 3 with their corresponding PLS parameters and preprocessing. The developed methods show low errors of cross-validation (RMSECV) (max. 1.38%) and high correlation coefficients of over 99.4%. The number of factors (principal components) of the PLS regression is also low, with values between 3 and 4.

3.4.2 | Validation of the developed methods

The developed methods were validated using the samples of the CO₂ exposure time experiments (Section 3.3) and statistical tests to determine if significant differences exist regarding the TG-FTIR reference method. The predicted and measured CaCO₃ contents as well as the relative errors regarding the reference method are illustrated in Figure 7 (Supplementary Material S5). The predicted values at lower CaCO₃ concentrations (20 wt%) are in good agreement with the reference method. However, the CaCO₃ content is underestimated for intermediate reference values and is significantly higher than the reference values at high CaCO₃ concentrations. The described trends are also represented in the relative errors regarding the reference values. Methods a and c show relative errors up to a maximum of 8–9%, while the relative errors at concentrations above 47 wt% are significantly higher. This could indicate that the number of data points in the calibration model is too low. According to Conzen,⁵⁶ the results of the PLS regression improve with an increasing number of data points in the data set. A paired *t*-test was used to evaluate if there is a significant difference between the predicted and the reference values. The prerequisite of normal distribution of the differences between the predicted and the reference values was verified with a Kolmogorov–Smirnov test ($\alpha = 0.01$). Since the calculated *p*-values of the paired *t*-test (method a: 0.526; method b: 0.241; method c: 0.730) are higher than the significance level of 0.05, the null

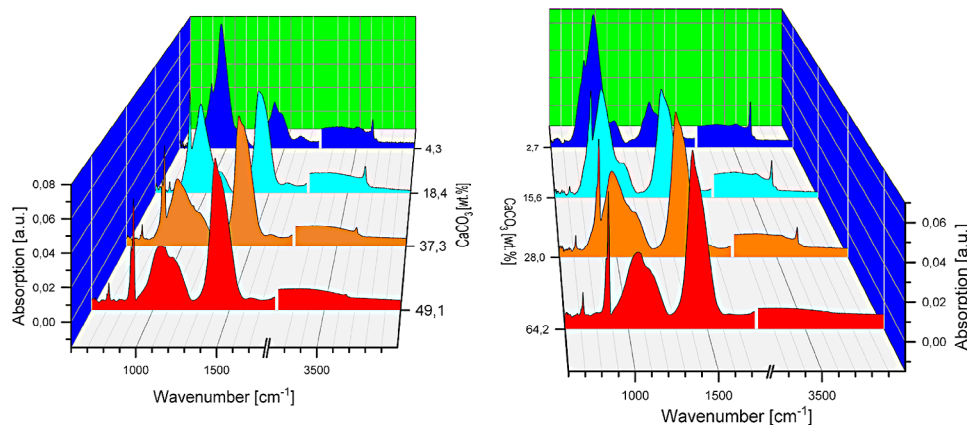


FIGURE 6 Evolution of the ATR-IR spectra as a function of the measured CaCO_3 content in the experiments on CO_2 exposure time (left) as well as the cement paste powder of the ATR-IR calibration mixtures (right).

TABLE 3 Developed ATR-IR methods and their parameters of the corresponding PLS regression.

Method	a	b	c
Preprocessing	SNV, SLS, MSC, 1.DER + SLS	LOS, SNV, MSC, 1.DER	MMN, SLS, MSC, 1.DER + SLS
Spectral ranges (cm^{-1})	683–1620	652–1266	
	3013–3683		
Factors	4	4	3
R^2	99.52	99.62	99.47
RMSECV (wt%)	1.38	1.1	1.34

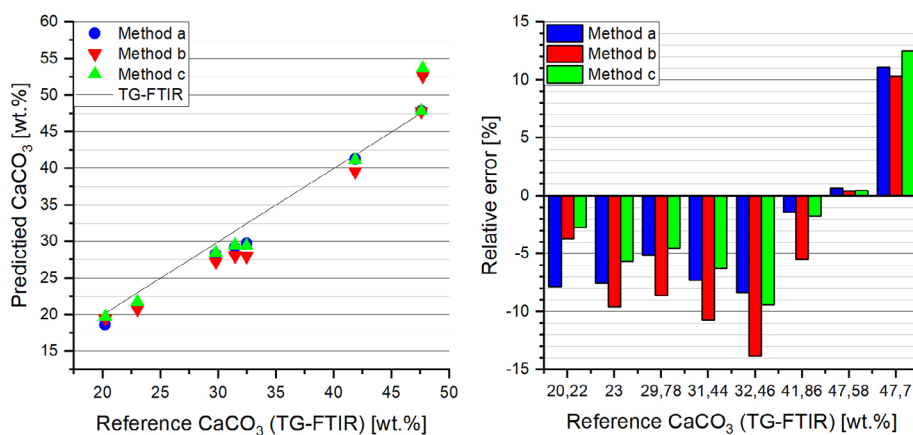


FIGURE 7 Comparison of the predicted CaCO_3 values of the developed ATR-IR methods and the TG-FTIR reference values (left) as well as the corresponding relative errors regarding the difference between predicted and reference values (right).

hypothesis cannot be discarded. Thus, there is no significant difference between the predicted and the reference values at a significance level of $\alpha = 0.05$ (Supplementary Material S6).

The precision of the developed and the reference methods was evaluated by investigating the variances

of six repeated measurements with an F -test. Two concentrations, 20 wt% and 48 wt% (V04 and V011) were investigated (predicted and reference values are listed in Supplementary Material S7). Before the F -test, the data sets were evaluated with a Grubbs test to eliminate the impact of potential outliers on the respective

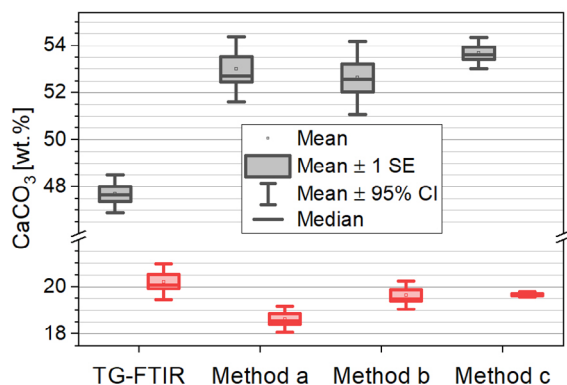


FIGURE 8 Boxplots of six repeated measurements of the developed ATR-IR methods and the TG-FTIR reference method in two concentration ranges (V11 as black and V04 as red symbols). The mean of the data set is represented as a line in the middle of a box, and the top and bottom of the box represent the standard deviation in terms of the standard error of the mean. The upper and lower edges of the whiskers bars represent the margins of the 95% confidence interval of the mean.

variances. The prerequisite of a normal distribution of the datasets for the Grubbs test and F -test were verified with a Kolmogorov–Smirnov test ($\alpha = 0.01$). The Grubbs test was applied ($\alpha = 0.01$) and one potential outlier (20.91 wt%) of method c was replaced with an additional measurement (19.82 wt%). Subsequently, no further outliers were found in the dataset and the datasets were normal-distributed ($\alpha = 0.01$); hence the F -test could be applied. Regarding sample V11, the F -test showed no significant difference between the developed and the reference methods (method a: $p = .250$, method b: $p = .169$, method c: $p = .724$; $\alpha = 0.05$). Regarding sample V04, the F -test showed no significant difference between method a as well as method b and the reference methods (method a: $p = .517$; method b: $p = .626$; $\alpha = 0.05$). However, the variances of sample V04 of method c showed a significant difference ($p = .0005$, $\alpha = 0.05$) regarding the reference values. Figure 8 illustrates the statistical parameters of the datasets as boxplots (Supplementary Material S8). Similar width of the boxes reflects the similarity between the variances of the developed ATR-IR and the TG-FTIR reference methods. Methods a and c show an even lower variance, that is, a higher precision at lower concentrations. The significant difference of the variance of sample V04 of method c can be seen very clearly. The box-plot illustration also exhibits that the confidence intervals of the ATR-IR methods at higher concentration do not overlap with the corresponding interval of the TG-FTIR method. To eliminate this discrepancy, the number of data points in the calibration data sets was increased in the subsequent optimization.

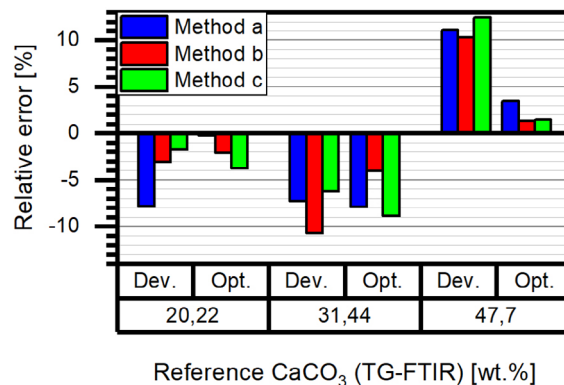


FIGURE 9 Relative errors of the developed as well as the optimized ATR-IR methods regarding the TG-FTIR reference.

3.4.3 | Method optimization

The optimization aimed to minimize the difference between the predicted values of the developed ATR-IR methods and the reference values of the TG-FTIR method. For this purpose, eight additional samples of the CO₂ exposure time experiments (Section 3.3) were added to the calibration data sets. The preprocessing of the methods remained unchanged, and the spectral ranges of the PLS regression were slightly adjusted and the number of factors (principal components) increased as illustrated in Table 4. The errors of cross-validation (RMSECV) of the optimized methods changed slightly while the correlation coefficients remained quite high between 99.4% and 99.7%. The optimized methods were validated in three concentration ranges (20, 31, and 48 wt% CaCO₃). To assess the impact of the optimization on the difference between the predicted and the reference values, the relative errors regarding the reference values are illustrated in Figure 9 (Supplementary Material S9). In general, the optimization led to a decrease in the relative errors of sample V04 (20 wt%) and sample V11 (48 wt%). Only for method c, a slight increase in errors is observed for sample V04. The relative error of sample V07 (31.44 wt%) decreased in method b while it slightly increased in method a and method c. This indicates that method b predicts the “best” results with the lowest deviation from the reference method. To reduce the deviation from the reference, it would be conceivable to develop multiple calibrations in different concentration ranges. Nevertheless, the relative errors of the optimized methods are below 5% for method b and 9% for methods a and c. This exhibits a high accordance between the optimized ATR-IR and the TG-FTIR reference methods.

The optimized methods were validated as described in Section 3.4.2. A paired t -test (method a: $p = .830$, method b: $p = .583$, method c: $p = .450$; $\alpha = 0.05$) and an F -test (V11:

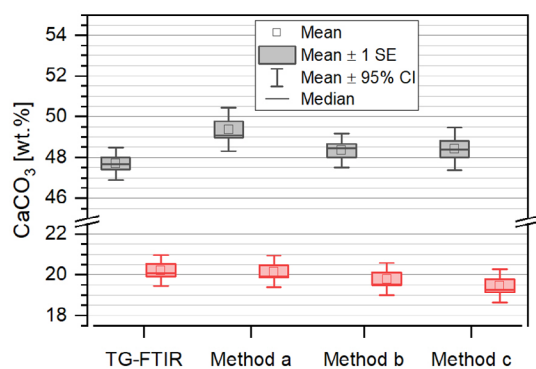
TABLE 4 Optimized ATR-IR methods and their parameters of the corresponding PLS regression.

Method	a	b	c
Preprocessing	SNV, SLS, MSC, 1.DER + SLS	LOS, SNV, MSC, 1.DER. + SLS	MMN, SLS, MSC, 1.DER + SLS
Spectral ranges (cm ⁻¹)	652–1638	652–1638	652–1638
	3013–3683	3601–3664	3013–3683
Factors	6	8	7
R ²	99.41	99.5	99.66
RMSECV (wt%)	1.46	1.29	1.1

TABLE 5 Comparison between the developed ATR-IR quantification methods and the reference methods.

Parameters	ATR-IR	TG	TG-FTIR
Sample preparation	Powder pressed to pellets	Powder in crucibles	Powder in crucibles
Duration of measurement	<3 min	~3 h	~3 h
Correlation coefficients	>99.4%	100%	100%
Reproducibility: e.s.d. of 6 measurements	<1.5 wt%	<1.8 wt%	<0.8 wt%
Concentration range of CaCO ₃	20–48 wt% (CO ₂ uptake of 19–56%)	0–100 wt%	0–100 wt% ^a
Restrictions	Limited to the spectrometer and cement used in the calibration	No distinct separation between CO ₂ and H ₂ O/SO ₃	universal applicability

^aPrerequisite: experimental parameters can be adjusted in correspondence to the validity of Lambert Beer's Law.

**FIGURE 10** Boxplots of six repeated measurements in two concentration ranges (V11 as black and V04 as red symbols, explanation in Figure 8).

method a: $p = .530$, method b: $p = .893$, method c: $p = .549$, $\alpha = 0.05$; V04: method a: $p = .982$, method b: $p = .945$, method c: $p = .885$, $\alpha = 0.05$) confirmed that there is no significant difference between predicted reference values and the variances, that is, the precision. No further outliers were found by the Grubbs test (Supplementary Material S10 and S11).

To emphasize the effects of the optimization, the statistical parameters of the data sets are illustrated in Figure 10 (Supplementary Material S12). In contrast to the first validation, all boxes show similar widths and therefore similar standard deviations/precisions of the individual methods.

The optimization also led to an overlap of the 95% confidence intervals of the mean of all optimized methods and the reference method. Thus, the developed and optimized ATR-IR methods show high accordance regarding the TG-FTIR reference method in a concentration range of 20–48 wt% CaCO₃.

4 | CONCLUSIONS

The carbonation of HCP prepared from CEM-I (Dyckerhoff white) was determined by TG, TG-FTIR, and ATR-IR. Results from accelerated carbonation of cylindrical slices of hardened cement paste (170°C and 8 bar) as a function of exposure time show that 60% of the CO₂ uptake occurred within the first 30 min and 90% within the first 60 min. The reduction of the carbonation rate with increasing carbonation time may be due to the formation of CaCO₃ layers that inhibit the diffusion of CO₂ and Ca²⁺ ions.⁵¹ Maximum CO₂ uptake was achieved by crushing the sample of hydrated cement paste before CO₂ exposure. After 52 h CO₂ exposure in the autoclave, the sample shows a CO₂ uptake efficiency of 77%–81% (TG-FTIR and TG).

Based on TG-FTIR data as a reference, PLS regression in conjunction with ATR-IR was used to develop three methods for the quantitative analysis of CaCO₃. The developed methods were validated, optimized, and validated once

again to evaluate the effects of the optimization. The basic parameters of the ATR methods, the TG-FTIR reference method, and TG are summarized in Table 5. The proposed and applied ATR-IR methods show great potential in the field of process control, where fast and precise quantitative measurements are a necessity to control and optimize production processes. They are characterized by high sensitivity to amorphous and crystalline CaCO_3 . However, ATR spectra are directly influenced by the C/S ratio of the HCP, the particle size, and the type of cement. In addition, these methods are limited to the analysis of amorphous CaCO_3 and calcite, the phases that were present in the calibration mixtures. Cement paste samples with an increased aragonite or vaterite content cannot be quantified reliably. Differences in the ATR-IR spectra of other CaCO_3 modifications would lead to false predictions of the PLS models. The previously described limitations of the ATR-IR methods could be reduced by extending the calibration data set in range, data points, and cement samples. The inclusion of different cement types, for example, blast furnace or pozzolan cement, and concrete mixtures in the PLS data sets could even enable the simultaneous analysis of several components as $\text{Ca}(\text{OH})_2$, individual CaCO_3 modifications, SiO_2 , CaSO_4 , bound water of the C-S-H, and the C/S ratio of the cements.

AUTHOR CONTRIBUTIONS

Conceptualization: J.K., A.U., K.G., D.M., P.S., and D.S. Formal analysis: J.K., A.U., D.M., and K.G. Investigation: J.K., A.U., D.M., and K.G. Writing—original draft preparation: J.K., A.U., and K.G. Writing—review and editing: P.S., D.M., and D.S. All authors have read and agreed to the published version of the manuscript.

ACKNOWLEDGMENTS

Many thanks go to Günter Beuchle, Britta Bergfeldt, Stefanie Kaufmann, and Julia Podszuweit for sample preparations and RFA measurements.

Open access funding enabled and organized by Projekt DEAL.

FUNDING

Program oriented funding of this work by the German Helmholtz Association in the frame of the Program “Materials and Technologies of the Energy Transition” is gratefully acknowledged.

CONFLICT OF INTEREST STATEMENT

The authors declare no conflicts of interest.

ORCID

Krassimir Garbev  <https://orcid.org/0000-0002-3303-5168>

REFERENCES

1. Scrivener KL, John VM, Gartner EM. Eco-efficient cements: potential economically viable solutions for a low- CO_2 cement-based materials industry. *Cem Concr Res*. 2018, 114:2–26. <https://doi.org/10.1016/j.cemconres.2018.03.015>
2. Scrivener KL, John VM, Gartner EM. Eco-efficient cements: potential economically viable solutions for a low- CO_2 cement-based materials industry. UNEP (United Nations Environment Program), Technical Report; 2016. <https://doi.org/10.25561/51016>
3. Scrivener KL, Martirena F, Bishnoi S, Maity S. Calcined clay limestone cements (LC3). *Cem Concr Res*. 2018, 114:49–56. <https://doi.org/10.1016/j.cemconres.2017.08.017>
4. Skocek J, Zajac M, Ben Haha M. Carbon capture and utilization by mineralization of cement pastes derived from recycled concrete. *Nat Sci Rep*. 2020, 10:5614. <https://doi.org/10.1038/s41598-020-62503-z>
5. Sanna A, Uibu M, Caramanna G, Kuusik R, Maroto-Valer MM. A review of mineral carbonation technologies to sequester CO_2 . *Chem Soc Rev*. 2014, 14:8049–80. <https://doi.org/10.1039/C4CS00035>
6. Favier A, De Wolf C, Scrivener KL, Habert G. A sustainable future for the European Cement and Concrete Industry: technology assessment for full decarbonisation of the industry by 2050. ETH Zurich. 2018. <https://doi.org/10.3929/ethz-b-000301843>
7. Zajac M, Skocek J, Ben Haha M, Deja J. CO_2 mineralization methods in cement and concrete industry. *Energies*. 2022, 15:3597. <https://doi.org/10.3390/en15103597>
8. Zajac M, Skocek J, Skibsted J, Ben Haha M. CO_2 mineralisation of demolished concrete wastes into a supplementary cementitious material- a new CCU approach for the cement industry. *RILEM Tech Lett*. 2021, 6:53–60. <https://doi.org/10.21809/rilemtechlett.2021.14>
9. Herterich J, Richardson J, Moro F, Marchi M, Black L. Microstructure and phase assemblage of low-clinker cements during the early stages of carbonation. *Cem Concr Res*. 2022, 152:106643. <https://doi.org/10.1016/j.cemconres.2021.10664>
10. Castellote M, Fernandez L, Andrade C, Alonso C. Chemical changes and phase analysis of OPC pastes carbonated at different CO_2 concentrations. *Mater Struct*. 2009, 42:515–25. <https://doi.org/10.1617/s11527-008-9399-1>
11. Sanna A, Uibu M, Caramanna C, Kuusik R, Maroto-Valer MM. A review of mineral carbonation technologies to sequester CO_2 . *Chem Soc Rev*. 2014, 43(23):8049–80. <https://doi.org/10.1039/C4CS00035H>
12. Suda Y, Tomiyama J, Saito T, Saeki T. Impact of relative humidity on carbonation shrinkage and microstructure of hardened cement paste. In: Proceedings of 6th International Conference on Construction Materials (ConMat'20). Fukuoka, Japan 27–29 August 2020. Tokyo: Japan Concrete Institute
13. Suda Y, Tomiyama J, Saito T, Saeki T. Phase assemblage, microstructure and shrinkage of cement paste during carbonation at different relative humidities. *J Adv Concr Technol*. 2021, 9(6):687–99. <https://doi.org/10.3151/jact.19.687>
14. Galan I, Andrade C, Mora P, Sanjuan MA. Sequestration of CO_2 by concrete carbonation. *Environ Sci Technol*. 2010, 44:3181–86. <https://doi.org/10.1021/es903581d>
15. Galan I, Andrade C, Castellote M. Natural and accelerated CO_2 binding kinetics in cement paste at different relative

- humidities. *Cem Concr Res.* 2013, 49:21–28. <https://doi.org/10.1016/j.cemconres.2013.03.009>
16. Klemm WA, Berger RL. Accelerated curing of cementitious systems by carbon dioxide: part I. Portland cement. *Cem Concr Res.* 1972, 2(5): 567–76. [https://doi.org/10.1016/0008-8846\(72\)90111-1](https://doi.org/10.1016/0008-8846(72)90111-1)
 17. Zhan BJ, Xuan DX, Poon CS, Shi CJ. Mechanism for rapid hardening of cement pastes under coupled CO₂-water curing regime. *Cem Concr Compos.* 2019, 97:78–88. <https://doi.org/10.1016/j.cemconcomp.2018.12.021>
 18. Liu Z, Meng W. Fundamental understanding of carbonation curing and durability of carbonation-cured cement-based composites: a review. *J CO₂ Util.* 2021, 44:101428. <https://doi.org/10.1016/j.jcou.2020.101428>
 19. Šavija B, Luković M. Carbonation of cement paste: understanding, challenges, and opportunities. *Constr Build Mater.* 2016, 117:285–301. <https://doi.org/10.1016/j.conbuildmat.2016.04.138>
 20. Black L, Garbev K, Gasharova B, Breen C, Yarwood J, Stemmermann P. Structural features of C-S-H(I) and its carbonation in air: a Raman spectroscopic study. Part II: Carbonated phases. *J Am Ceram Soc.* 2007, 90(3):908–17. <https://doi.org/10.1111/j.1551-2916.2006.01429.x>
 21. Sevelsted TF, Skibsted J. Carbonation of C-S-H and C-A-S-H samples studied by ¹³C, ²⁷Al and ²⁹Si MAS NMR spectroscopy. *Cem Concr Res.* 2015, 71:56–65. <https://doi.org/10.1016/j.cemconres.2015.01.019>
 22. Ashraf W. Carbonation of cement-based materials: challenges and opportunities. *Constr Build Mater.* 2016, 120:558–70. <https://doi.org/10.1016/j.conbuildmat.2016.05.080>
 23. Shi Z, Lothenbach B, Geiker MR, Kaufmann J, Leemann A, Ferreiro S, et al. Experimental studies and thermodynamic modeling of the carbonation of Portland cement, metakaolin and limestone mortars. *Cem Concr Res.* 2016, 88:60–72. <https://doi.org/10.1016/j.cemconres.2016.06.006>
 24. Groves, GW, Brough, A, Richardson, IG, Dobson, CM. Progressive changes in the structure of hardened C₃S cement pastes due to carbonation. *J Am Ceram Soc.* 1991, 74:2891–96. <https://doi.org/10.1111/j.1151-2916.1991.tb06859.x>
 25. Taylor HWF. *Cement Chemistry* (2nd ed.). London: Thomas Telford, 1997.
 26. Merz D, Dregert O, Garbev K, Stemmermann P. A reliable quantitative TA-FTIR method for cementitious material characterization. Proceedings of GEFTA-STK-joint Meeting on Thermal Analysis and Calorimetry. Vortrag. 2012; 53.
 27. Rodriguez-Blanco JD, Shaw S, Benning LG. The kinetics and mechanisms of amorphous calcium carbonate (ACC) crystallization to calcite, via vaterite. *Nanoscale.* 2011, 3:265–71. <https://doi.org/10.1039/C0NR00589D>
 28. Vagenas NV, Gatsouli A, Kontoyannis CG. Quantitative analysis of synthetic calcium carbonate polymorphs using FT-IR spectroscopy. *Talanta.* 2003, 59(4):831–36. [https://doi.org/10.1016/S00399140\(02\)00638-0](https://doi.org/10.1016/S00399140(02)00638-0)
 29. Horgnies M, Chen JJ, Bouillon C. Overview about the use of Fourier Transform Infrared spectroscopy to study cementitious materials. *WIT Trans Eng Sci.* 77:2013, 251–62. ISSN 1743–3533.
 30. Higl J, Hinder D, Rathgeber C, Ramming B, Lindén M. Detailed in situ ATR-FTIR spectroscopy study of the early stages of C-S-H formation during hydration of monoclinic C₃S. *Cem Concr Res.* 2021, 142:106367. <https://doi.org/10.1016/j.cemconres.2021.106367>
 31. John E, Stephan D. Calcium silicate hydrate in-situ development of the silicate structure followed by infrared spectroscopy. *J Am Ceram Soc.* 2021, 104:6611–24. <https://doi.org/10.1111/jace.18019>
 32. Mendes dos Santos VHJ, Pontin D, Ponzi GGD, de Guimarães e Stepanha AS, Martel RB, Schütz MK, et al. Application of Fourier Transform infrared spectroscopy (FTIR) coupled with multivariate regression for calcium carbonate (CaCO₃) quantification in cement. *Constr Build Mater.* 2021, 313:125413. <https://doi.org/10.1016/j.conbuildmat.2021.125413>
 33. Black L, Stumm A, Garbev K, Stemmermann P, Hallam KR, Allen GC. X-ray photoelectron spectroscopy of the cement clinker phases calcium trisilicate and β-calcium disilicate. *Cem Concr Res.* 2003, 33(10):1561–65. [https://doi.org/10.1016/S0008-8846\(03\)00097-8](https://doi.org/10.1016/S0008-8846(03)00097-8)
 34. Rodriguez ET, Garbev K, Merz D, Black L, Richardson IG. Thermal stability of C-S-H phases and applicability of Richardson and Groves' and Richardson C-(A)-S-H(I) models to synthetic C-S-H. *Cem Concr Res.* 2017, 93:45–56. <https://doi.org/10.1016/j.cemconres.2016.12.005>
 35. Scrivener K, Snellings R, Lothenbach B. *A Practical Guide to Microstructural Analysis of Cementitious Materials.* Boca Raton: Taylor and Francis. 2017; ISBN: 9781138747234. <https://doi.org/10.1201/b19074>
 36. Chang C-F, Chen J-W. The experimental investigation of concrete carbonation depth. *Cem Concr Res.* 2006, 36(9):1760–67. <https://doi.org/10.1016/j.cemconres.2004.07.025>
 37. Whittaker M, Dubina E, FAI-Mutawa F, Arkless L, Plank J, Black L. The effect of prehydration on the engineering properties of CEM I Portland cement. *Adv Cem Res.* 2013, 25(1):12–20. <https://doi.org/10.1680/adcr.12.00030>
 38. Yu P, Kirkpatrick RJ, Poe B, McMillan PF, Cong X. Structure of calcium silicate hydrate (C-S-H): near, mid and far-infrared spectroscopy. *J Am Ceram Soc.* 1999, 82:742–48. <https://doi.org/10.1111/j.1151-2916.1999.tb01826.x>
 39. Ylmén R, Jäglid U, Panas I. Monitoring early hydration of cement by ex situ and in situ ATR-FTIR—a comparative study. *J Am Ceram Soc.* 2014, 97(11):3669–75. <https://doi.org/10.1111/jace.13186>
 40. Shao Y, Rostami V, He Z, Boyd AJ. Accelerated carbonation of Portland limestone cement. *J Mat Civil Eng.* 2014, 26(1):117–24. [https://doi.org/10.1061/\(ASCE\)MT.1943-5533.0000773](https://doi.org/10.1061/(ASCE)MT.1943-5533.0000773)
 41. Mollah MYA, Yu W, Schennach R, Cocke DL. A Fourier transform infrared spectroscopic investigation of the early hydration of Portland cement and the influence of sodium lignosulfonate. *Cem Concr Res.* 2000, 30:267–73. [https://doi.org/10.1016/S0008-8846\(99\)00243-4](https://doi.org/10.1016/S0008-8846(99)00243-4)
 42. Fernandez-Carrasco L, Torrens-Martin D, Morales LM, Martinez-Ramirez S. Infrared spectroscopy in the analysis of building and construction materials. In: T. Theophanides (Ed.), *Infrared Spectroscopy-Materials science, Engineering and Technology.* InTech. 2012, 369–82.
 43. Steiner S, Lothenbach B, Proske T, Borgschulte A, Winnefeld F. Effect of relative humidity on the carbonation rate of portlandite, calcium silicate hydrates and ettringite. *Cem Concr Res.* 2020, 135:106116.
 44. Andersen FA, Brecevic L. Infrared spectra of amorphous and crystalline calcium carbonate. *Acta Chem Scand.* 1991, 45:1018–24. <https://doi.org/10.3891/acta.chem.scand.45-1018>

45. Trezza MA, Lavat AE. Analysis of the system $3\text{CaO}\cdot\text{Al}_2\text{O}_3\text{-CaSO}_4\cdot 2\text{H}_2\text{O-CaCO}_3\pm\text{H}_2\text{O}$ by FT-IR spectroscopy. *Cem Concr Res.* 2001, 31(3):869–72. [https://doi.org/10.1016/S0008-8846\(01\)00502-6](https://doi.org/10.1016/S0008-8846(01)00502-6)
46. Legodi MA, de Waal D, Potgieter JH. Quantitative determination of CaCO_3 in cement blends by FT-IR. *Appl Spectrosc.* 2001, 55(3):361–65.
47. Sterzel W. Der Einfluß der Kristallstruktur auf die Kopplung der ν_2 Schwingung von Carbonationen. *Z Anorg Allg Chem.* 1969, 368:308–16. <https://doi.org/10.1002/zaac.19693680512>
48. Carteret C, De La Pierre M, Dossot M, Pascale F, Erba A, Dovesi R. The vibrational spectrum of CaCO_3 aragonite: a combined experimental and quantum-mechanical investigation. *J Chem Phys.* 2013, 138:014201 <https://doi.org/10.1063/1.4772960>
49. Valenzano L, Torres FJ, Doll K, Pascale F, Zicovich-Wilson CM, Dovesi R. *Ab initio* study of the vibrational spectrum and related properties of crystalline compounds; the case of CaCO_3 calcite. *Z Phys Chem.* 2006, 220(7):893–912. <https://doi.org/10.1524/zpch.2006.220.7.893>
50. Huntzinger DN, Gierke JS, Kawatra SK, Eisele TC, Sutter LL. Carbon dioxide sequestration in cement kiln dust through mineral carbonation. *Environ Sci Technol.* 2009, 43(6):1986–92. <https://doi.org/10.1021/es802910z>
51. Fang Y, Chang J. Microstructure changes of waste hydrated cement paste induced by accelerated carbonation. *Constr Build Mater.* 2015, 76:360–65. <http://dx.doi.org/10.1016/j.conbuildmat.2014.12.017>
52. Wang T, Huang H, Huang X, Hu X, Fang M. Accelerated mineral carbonation curing of cement paste for CO_2 sequestration and enhanced properties of blended calcium silicate. *Chem Eng J.* 2017, 323:320–29. <https://doi.org/10.1016/j.cej.2017.03.157>
53. Morandea A, Thiery M, Dangla P. Investigation of the carbonation mechanism of {CH} and C-S-H in terms of kinetics, microstructure changes and moisture properties. *Cem Concr Res.* 2014, 56:153–70. <https://doi.org/10.1016/j.cemconres.2013.11.015>
54. Kanshef-Haghighi S, Ghoshal S. Physico-chemical processes limiting CO_2 uptake in concrete during accelerated carbonation curing. *Ind Eng Chem Res.* 2013, 52(16):5529–37. <https://doi.org/10.1021/ie303275e>
55. Jang JG, Kim GM, Kim HJ, Lee HK. Review on recent advances in CO_2 utilization and sequestration technologies in cement-based materials. *Constr Build Mater.* 2016, 127:762–73. <https://doi.org/10.1016/j.conbuildmat.2016.10.017>
56. Conzen JP. *Multivariate Kalibration: ein praktischer Leit-faden zur Methodenentwicklung in der quantitativen Analytik.* Bruker Optik. 2005, ISBN: 9783929431131

SUPPORTING INFORMATION

Additional supporting information can be found online in the Supporting Information section at the end of this article.

How to cite this article: Kalkreuth J, Ullrich A, Garbev K, Merz D, Stemmermann P, Stapf D. Accelerated carbonation of hardened cement paste: Quantification of calcium carbonate via ATR infrared spectroscopy. *J Am Ceram Soc.* 2023;1–14. <https://doi.org/10.1111/jace.19546>